

SiO collimated outflows driven by high-mass YSOs in G24.78+0.08

Codella C.^{1,2}, Beltrán M.T.¹, Cesaroni R.¹, Moscadelli L.¹, Neri R.³, Vasta M.¹, and Zhang Q.⁴

¹ INAF, Osservatorio Astrofisico di Arcetri, Largo E. Fermi 5, I-50125 Firenze, Italy

² UJF-Grenoble 1 / CNRS-INSU, Institut de Planétologie et d'Astrophysique de Grenoble (IPAG) UMR 5274, Grenoble, F-38041, France

³ IRAM, 300 rue de la Piscine, 38406 Saint Martin d'Hères, France

⁴ Harvard-Smithsonian Center for Astrophysics, 60 Garden Street, Cambridge MA 02138, USA

Received date; accepted date

ABSTRACT

Context. The region G24.78+0.08, which is associated with a cluster of high-mass young stellar objects in different evolutionary stages, is one of the best laboratories to investigate massive star-formation.

Aims. We aim to image the molecular outflows towards G24.78+0.08 at high-angular resolution using SiO emission, which is considered the classical tracer of protostellar jets. In this way we study the mass loss process in which we previously detected a hypercompact ionised region, as well as rotation and infall signatures.

Methods. We performed SiO observations with the VLA interferometer in the $J = 1-0 \nu=0$ transition and with the SMA array in the 5–4 transition. A complementary IRAM 30-m single-dish survey in the (2–1), (3–2), (5–4), and (6–5) SiO lines was also carried out.

Results. Two collimated SiO high-velocity (up to 25 km s⁻¹ w.r.t. the systemic velocity) outflows driven by the A2 and C millimeter continuum massive cores have been imaged. On the other hand, we detected no SiO outflow driven by the young stellar objects in more evolved evolutionary phases that are associated with ultracompact (B) or hypercompact (A1) HII regions. The A2 outflow has also been traced using H₂S. The LVG analysis of the SiO emission reveals high-density gas (10³–10⁴ cm⁻³), with well constrained SiO column densities (0.5–1 10¹⁵ cm⁻²). The driving source of the A2 outflow is associated with typical hot core tracers such as CH₃OCHO (methyl formate), C₂H₃CN (vinyl cyanide), HCC¹³CN (cyanoacetylene), and (CH₃)₂CO (acetone).

Conclusions. The driving source of the main SiO outflow in G24 has an estimated luminosity of a few 10⁴ L_⊙ (typical of a late O-type star) and is embedded in the 1.3 mm continuum core A2, which in turn is located at the centre of a hot core that rotates on a plane perpendicular to the outflow main axis. The present SiO images support a scenario similar to the low-mass case for massive star formation, where jets that are clearly traced by SiO emission, create outflows of swept-up ambient gas usually traced by CO.

Key words. ISM: individual objects: G24.78+0.08 — ISM: molecules — stars: formation

1. Introduction

Two main theoretical scenarios, based on accretion, are proposed to explain the formation of O-B type stars: (i) the core accretion model (McKee & Tan 2002, 2003), where massive stars form from massive cores, and (ii) the competitive accretion model (Bonnell et al. 2007), where a molecular cloud fragments into low-mass cores, which form stars that compete to accrete mass from a common gas reservoir. Both models predict the existence of accretion disks around massive young stellar objects (YSOs), and the presence of jets driving molecular outflows. The core accretion model is a scaled-up scenario of low-mass star formation. The competitive accretion model suggests that massive stars always form in densely clustered environments and that disks and collimated jets are perturbed by interaction with stellar companions. Observation of YSOs with disk/jet systems, and of their properties, would help to distinguish between models.

The region G24.78+0.08 (hereafter G24), located at 7.7 kpc from the Sun, is one of the best laboratories to investigate the process of massive star formation. Several observational campaigns were performed with single-dish antennas and interferometers (Codella et al. 1997; Furuya et al. 2002; Cesaroni et al. 2003; Beltrán 2004, 2005, 2006, 2007, 2011; Moscadelli et al. 2007; Vig et al. 2008) toward this region. G24 is associated with a cluster of high-mass YSOs in different evolutionary stages, distributed in a region with size $\sim 10''$ (see YSOs labelled

A1, A2, B, C, and D in Fig. 1). Beltrán et al. (2005, 2011) resolved A1 and A2 into five cores (see labels in Fig. 2) aligned in a southeast-northwest direction, which suggests a preferential direction for star formation in this region. The A cores are embedded in huge (0.1 pc), massive (a few 100 M_⊙) toroids, that rotate around the southeast-northwest (SE-NW) direction, and could still host elusive accretion disks in their interior (Beltrán et al. 2005). This possibility would be even more intriguing for the object labelled A1, which is unique, because of the simultaneous presence of almost all the "ingredients" expected in a typical star formation "recipe": a 20 M_⊙ star surrounded by a hypercompact HII region, that is located at the centre of a rotating toroid undergoing infall towards the star. The association of the rotation of toroids with the coherent motion of accretion disks would be supported by the detection of outflows, possibly driven by jets, along the SE-NW direction. The occurrence of outflows towards A and C has been first reported by Furuya et al. (2002) and has recently been imaged by Beltrán et al. (2011) at high-angular resolution using CO emission. In particular, Beltrán et al. (2011) suggested that A2, and not A1, is the driving source of a bipolar CO outflow located along the SE-NW direction. However, given the complex outflow structure towards cores A1 and A2, we cannot entirely discard the possibility that the core A1 could be powering an additional outflow in the region.

This doubt calls for high-angular resolution observations of a reliable jet tracer. Silicon monoxide (SiO) thermal emission

is the best tool for this purpose: unlike other species such as CO, it is associated with shocks inside jets, suffers minimal contamination from infalling envelopes or swept-up cavities, and traces regions close to protostars, which are heavily extinguished even in the near- and mid-infrared regions (e.g. Codella et al. 2007; Lee et al. 2007a). Only SiO line emission will allow us to probe the mass loss process and unambiguously determine the direction of the flows driven by the G24 cluster. The formation of SiO is attributed to the sputtering of Si atoms from charged grains in a magnetised C-shock with velocities higher than 20 km s^{-1} (Schilke et al. 1997; Gusdorf et al. 2008ab). Although high-angular resolution studies of SiO in high-mass star-forming regions still refer to a quite limited number of objects (Hunter et al. 1999; Cesaroni et al. 1999; Qiu et al. 2007; Zhang et al. 2007), they confirm the power of SiO in tracing the mass loss process in complex environments like those typical of the massive star-forming regions.

In this paper, we present SiO(1–0) and SiO(5–4) images obtained with the NRAO¹ Very Large Array (VLA) and SubMillimeter Array (SMA)² as well as a complementary IRAM³ 30-m observations to unveil the mass loss process driven by the G24 cluster of high-mass YSOs.

2. Observations

2.1. VLA

The G24 cluster was observed with 27 antennas of the NRAO VLA to measure the SiO(1–0) line emission at 43.4 GHz as well as the continuum emission. The observations were carried out in the Q-band with the D-configuration on August 10, 2008, and October 10, 2009, and with the C-configuration on August 14, 2009. The half power beam width (HPBW) of the antennas is $\sim 1'$, which is the field-of-view of the images. The largest structure visible in the C+D-configuration is $\sim 43''$. The phase reference centre of the observations was set to $\alpha_{2000} = 18^{\text{h}} 36^{\text{m}} 12^{\text{s}}.660$, $\delta_{2000} = -07^{\circ} 12' 10''.15$.

The SiO(1–0) line and the continuum were observed simultaneously with the correlator in 2 IF mode. The continuum emission was collected with a 200 MHz bandwidth centred at 43.339 GHz. The SiO(1–0) line was covered by simultaneously using two slightly overlapping 6.25 MHz (43 km s^{-1}) bands⁴. Unfortunately, technical problems did not allow us to properly trace the SiO(1–0) emission in the VLA–D configuration. The observations were performed in fast-switching mode. Bandpass and phase were calibrated by observing 1832–105, while the flux density scale was derived by observing 1331+305 (3C286). All data editing and calibration were carried out using the NRAO AIPS⁵ package. The line cubes were obtained by subtracting the continuum from the line. Images were produced using natural weighting: Details of the synthesised cleaned beam, spectral resolution, and rms noise of the maps are given in Table 1.

¹ The National Radio Astronomy Observatory is a facility of the National Science Foundation operated under cooperative agreement by Associated Universities, Inc

² The SubMillimeter Array is a joint project between the Smithsonian Astrophysical Observatory and the Academia Sinica Institute of Astronomy and Astrophysics, and is funded by the Smithsonian Institution and the Academia Sinica.

³ IRAM is supported by INSU/CNRS (France), MPG (Germany), and IGN (Spain).

⁴ The 12.5 MHz bandwidth, needed to cover the whole SiO(1–0) profile, was not available during the observations.

⁵ <http://www.aips.nrao.edu/index.shtml>

2.2. SMA

The target was observed in the SiO(5–4) line at 217.1 GHz and in the continuum at 1.4 mm with the SMA using two different array configurations. Compact- and extended-array observations were taken on May 21 and July 19, 2008, respectively. The covered baselines have lengths between ~ 8 and 100 k λ (compact) and 17 and 160 k λ (extended). We used two spectral sidebands, both 2 GHz wide, separated by 10 GHz, covering the frequency ranges of 215.4–217.4 and 225.4–227.4 GHz, with a uniform spectral resolution of about 0.5 km s^{-1} . The phase reference centre of the observations was set to $\alpha_{2000} = 18^{\text{h}} 36^{\text{m}} 12^{\text{s}}.565$, $\delta_{2000} = -07^{\circ} 12' 10''.90$.

Absolute flux calibration was derived from observations of Titan and Uranus. The bandpass of the receiver was calibrated by observations of the quasars 3C279 and 3C454.3. Amplitude and phase calibrations were achieved by monitoring 1743–038 and 1911–201. We estimated the flux-scale uncertainty to be better than 15%. The visibilities were calibrated with the IDL superset MIR⁶. Additional imaging and analysis was performed with MIRIAD (Sault et al. 1995) and GILDAS⁷. The continuum was constructed in the (u,v)-domain from the line-free channels both in the LSB and USB. Continuum maps were created by combining the data of both compact and extended configurations with the ROBUST parameter of Briggs (1995) set equal to zero, whereas SiO(5–4) line channel maps were created using natural weighting after continuum subtraction in the UV plane. Angular and spectral resolution and as map sensitivity are given in Table 1.

2.3. IRAM 30-m

Single-dish observations to prepare the interferometric observational campaign were obtained with the IRAM 30-m telescope at Pico Veleta (Granada, Spain). The observations were carried out on January 27, 2007 pointing the telescope towards the position used as phase centre for the SMA observations: $\alpha_{2000} = 18^{\text{h}} 36^{\text{m}} 12^{\text{s}}.565$, $\delta_{2000} = -07^{\circ} 12' 10''.90$. The pointing was checked by observing nearby planets or continuum sources and was found to be accurate to within 3–4''. The observations were made by position-switching in wobbler mode. As spectrometer, an autocorrelator split into different parts was used to allow simultaneous observations of four lines: SiO(2–1) at 86.8, (3–2) at 130.3, (5–4) at 217.1, and (6–5) at 260.5 GHz, respectively (see Fig. 3). The angular (HPBW) and the velocity resolutions provided by the backend, and the reached sensitivities are shown in Table 1. The integration time (ON+OFF source) was 70 minutes, while the main beam efficiency varies from about 0.77 (at 87 GHz) to 0.48 (at 260 GHz). The spectra were calibrated with the standard chopper wheel method (uncertainty $\sim 10\%$) and are reported here in units of main-beam temperature (T_{MB}).

3. Results

3.1. Continuum emission

Figure 1 shows the VLA and SMA maps of the continuum emission at 7 and 1.4 mm, respectively, towards G24. Table 2 summarises the position and the peak intensity of the detected cores. Given the lower angular-resolution, the present continuum image at 1.4 mm does not add information with respect to our previous PdBI and SMA observations at similar wavelengths (1.3–

⁶ <http://cfa-www.harvard.edu/cqi/mircook.html>

⁷ <http://www.iram.fr/IRAMFR/GILDAS>

Table 1. List of the continuum and SiO observations

Observation	Telescope	ν^a (GHz)	E_u^a (K)	$S\mu^{2a}$ (D ²)	HPBW (arcsec)	PA (deg)	Spectral resolution (km s ⁻¹)	rms noise ^b (mJy beam ⁻¹)	(mK)
continuum	VLA-C+D	43.339	–	–	1.5 × 1.1	–11	–	0.8	309
continuum	SMA	219.601	–	–	1.5 × 1.4	74	–	6.0	72
SiO(1–0)	VLA-D ^c	43.424	2	9.6	2.2 × 1.7 ^c	–15 ^c	0.67	5	870
SiO(2–1)	IRAM-30m	86.847	6	19.3	28	–	0.54	77	16
SiO(3–2)	IRAM-30m	130.269	13	28.9	19	–	0.36	90	18
SiO(5–4)	IRAM-30m	217.105	31	48.1	11	–	0.43	173	37
SiO(5–4)	SMA	217.105	31	48.1	1.7 × 1.4	67	0.67	36	415
SiO(6–5)	IRAM-30m	260.518	44	57.7	9	–	0.36	189	42

^a Frequencies and spectroscopic parameters of the molecular transitions have been extracted from the Jet Propulsion Laboratory molecular database (Pickett et al. 1998). ^b For the molecular line observations the 1 σ noise is given per channel. ^c The SiO(1–0) emission has been successfully observed only with the VLA–D configuration.

Table 2. Position and peak intensity of the continuum cores^a

Core	α (J2000) (h m s)	δ (J2000) ($^\circ$ ' '')	$I_{7\text{mm}}^{\text{peak}}$ (mJy beam ⁻¹)	$I_{1.4\text{mm}}^{\text{peak}}$ (mJy beam ⁻¹)
G24 A1	18 36 12.55	–07 12 11.05	69	422
G24 B	18 36 12.65	–07 12 15.02	12	–
G24 C	18 36 13.11	–07 12 07.42	–	95
G24 D	18 36 12.17	–07 12 06.15	–	22

^a The positions are based on the SMA image for all sources but B, which is detected only with the VLA.

Table 3. Positions of the SiO emission peaks in the VLA and SMA images

Peak	α (J2000) (h m s)	δ (J2000) ($^\circ$ ' '')
SiO(1–0) – VLA		
Red	18 36 12.55	–07 12 10.54
Blue ^a	18 36 12.52	–07 12 09.12
SiO(5–4) – SMA		
Red	18 36 12.56	–07 12 10.50
Blue	18 36 12.45	–07 12 10.30

^a The SiO(1–0) blue-shifted emission is affected by absorption at low-velocities (see text).

Table 4. List of the species and transitions serendipitously detected

Transition	ν^a (GHz)	E_u^a (K)	$S\mu^{2a}$ (D ²)
C ₂ H ₅ CN(10 _{1,10} –9 _{1,9})	86.820	24	0.5
(CH ₃) ₂ CO(18 _{4,14} –17 _{5,13})-AE	215.881	111	655.7
¹³ CH ₃ OH-E(4 _{2,2} –3 _{1,2})	215.887	45	3.5
CH ₃ OCHO-E(20 _{1,20} –19 _{1,19})	215.892	298	53.0
CH ₃ OCHO-A(19 _{2,18} –18 _{1,17})	216.360	109	7.2
¹³ CH ₃ OH-A(10 _{2,9} –9 _{3,6})	216.370	162	2.7
H ₂ S(2 _{2,0} –2 _{1,1})	216.710	84	2.0
C ₂ H ₃ CN(23 _{2,22} –22 _{2,21})	216.937	134	996.4
CH ₃ OH-E(5 _{1,4} –4 _{2,2})	216.946	56	1.1
CH ₃ OCHO-E(17 _{3,14} –16 _{3,13})	216.959	286	43.7
CH ₃ OCHO-E(20 _{1,20} –19 _{1,19})	216.965	111	52.8
CH ₃ OCHO-A(20 _{1,20} –19 _{1,19})	216.966	111	52.8
¹³ CH ₃ OH-A(10 _{2,8} –9 _{3,7})	217.400	162	2.7
HCC ¹³ CN(24–23)	217.420	130	346.4
C ₂ H ₅ CN(29 _{5,25} –28 _{5,24})	260.536	215	417.0

^a Frequencies and spectroscopic parameters of the molecular transitions have been extracted from the Jet Propulsion Laboratory molecular database (Pickett et al. 1998) for all transitions except those of methanol, which have been extracted from the Cologne Database for Molecular Spectroscopy (Müller et al. 2005).

1.4 mm; Beltrán et al. 2005, 2011), which are consistent with the new observations. On the other hand, the present VLA beam is slightly better than that of our previous observations at 7 mm (2'3×1'7, Furuya et al. 2002), but the sensitivity is a factor 2 lower. Again, the present VLA results agree with the previously performed analysis. The source B has been detected at 7 mm and not at 1.4 mm is consistent with its evolved stage, which is associated with an ultra compact (UC) HII region (see e.g. Furuya et al. 2002). But the analysis of the continuum emission is beyond the scope of the present paper, and will not be further pursued.

3.2. SiO outflows

The outflow activity was previously detected using emission of CO isotopologues by Furuya et al. (2002) and Beltrán et al. (2011) with the PdBI and SMA interferometers. Two molecular outflows, both oriented in the northwest-southeast direction, were imaged. One (hereafter called outflow A) associated with the region of the A1+A2 cores and is probably driven by A2. Another bipolar outflow is associated with core C. Figure 2 shows the maps of the integrated blue- and red-shifted SiO(1–0) emission observed with the VLA in the D configuration towards the G24 cluster, while Fig. 4 shows examples of the SiO(1–0) profiles observed towards the positions of A1 and of the blue- and red-shifted SiO(1–0) emission peaks of the outflow A (see Table 3). The cloud systemic velocity is +111 km s⁻¹, according to Furuya et al. (2002). The SiO(1–0) lines are characterised by emission up to high velocities (\sim 20–25 km s⁻¹ with respect to the cloud velocity) in the wings, i.e. velocities comparable with what is observed using CO isotopologues. For outflow A, the VLA data confirm a poorly collimated and extended blue-shifted NW lobe and a smaller and more collimated red-shifted SE lobe. As seen in CO (Beltrán et al. 2011), each lobe is characterised by the presence of a weaker extended counter-lobe. This could be a geometry effect because outflow A's main axis lies close to the plane of the sky. Alternatively, this could reflect the occurrence of a second outflow. For outflow C, the SiO(1–0) map shows a very elongated red-shifted (\sim 25 km s⁻¹ w.r.t. the systemic velocity) lobe: by dividing the length of the outflow by its width, we derive a collimation factor $f_c \sim 4$. In this case, we detect no SiO blue-shifted emission, whereas the CO data of Beltrán et al. (2011) clearly show blue lobe, albeit smaller (by a factor 3) than the red lobe. This suggests that outflow C could be located close to the edge of the molecular cloud and therefore the blue-shifted gas could flow through a low-density region. This could also explain the lack of SiO emission, which is expected to trace the high-density collimated wind from the YSO.

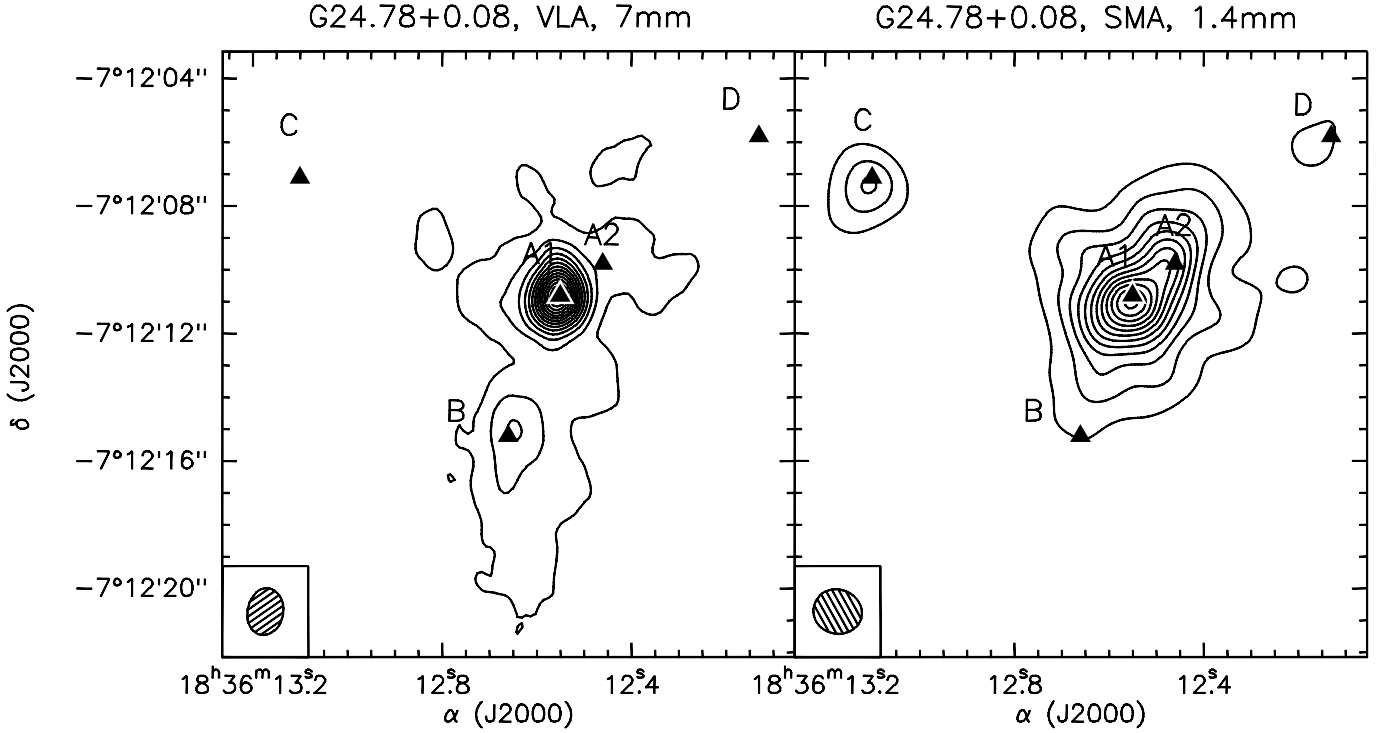


Fig. 1. Contour plots of the continuum emission at 7 (left panel) and 1.4 mm (right panel) imaged with the VLA and SMA interferometers, respectively. The black triangles mark the positions of the sources identified by Furuya et al. (2002) and Beltrán et al. (2004). The 1σ rms of the maps is 6.0 (at 1.4 mm) and 0.8 mJy beam⁻¹ (at 7 mm), while first contours and steps correspond to 3σ and 6σ . The ellipses in the bottom-left corners show the HPBW: $1''.5 \times 1''.4$ (PA = 74°; SMA) and $1''.5 \times 1''.1$ (PA = -11°; VLA).

Finally, no outflow activity has ever been observed towards source B, in agreement with its evolved stage, which is associated with an UCHII region (Codella et al. 1997; Furuya et al. 2002). No SiO emission (or CO emission) has been detected towards core D, which remains the most enigmatic object, because it is traced only by $\sim 1\text{--}3$ mm continuum emission and is not detected in any molecule (Furuya et al. 2002; Beltrán et al. 2011). Our non-detection seems to confirm that D is a non-centrally-peaked core without active star formation.

The VLA image of the low-excitation ($E_u = 2$ K) SiO(1–0) emission is affected by absorption features⁸, which prevents us from drawing a definite picture of the morphology of the SiO outflow and from identifying the driving source. Figure 5 shows a zoom-in of the central region of G24.78+0.08, centred on the cluster of the A1–A2 continuum sources. The green contours correspond to the narrow absorption blue-shifted feature (from +106 to +110 km s⁻¹, see Fig. 4) observed towards A1, against the hypercompact HII region imaged by Beltrán et al. (2007). This is ionised by a zero-age main-sequence star of spectral type O9.5 and mass of about 20 M_\odot . The hypercompact HII region is very bright and therefore it is expected to observe colder molecular gas in absorption against it. Indeed, at cm-wavelengths, where the brightness temperature of A1 is $\sim 5 \times 10^3$ K in a $\sim 0''.8$ beam (Beltrán et al. 2007), the NH₃(2,2) spectral pattern has allowed us to trace the blue-shifted outflow lobe and the red-shifted gas infalling towards A1 in absorption (Beltrán et al. 2006). In conclusion, the VLA SiO(1–0) map calls for the spectral analysis of a higher-J SiO at higher frequencies,

⁸ Unfortunately, we lack the information on the SiO velocity between +111 and +113 km s⁻¹ towards the position of A1 because of technical problems.

than those observed at SMA, where the brightness of the A1 hypercompact HII can be neglected.

Figure 6 shows the SMA maps of the integrated blue- and red-shifted SiO(5–4) emission. Only a hint of the outflow C is seen, and, as in the case of SiO(1–0), no emission has been observed towards cores B and D. On the other hand, the bipolar outflow A is clearly imaged, with the emission peaks lying closer to the A1+A2 system. The SiO(5–4) structure is consistent with that traced by the SiO(1–0) line. Table 3 reports the positions of the SiO emission peaks detected in the VLA and SMA images. The position of the red-shifted peak is basically the same (within the uncertainties) for the SiO(1–0) and (5–4) lines, whereas, given the absorption observed at low velocities that affects the SiO(1–0) map (see Fig. 4), the positions of the blue-shifted peaks in the two lines differ by $\sim 1''.6$. Example of SiO(5–4) spectra are shown in Fig. 4.

Figure 7 shows the maps of the SiO(5–4)/SiO(1–0) intensity ratio, obtained after smoothing the maps to the same angular resolution, and derived where both emissions have a signal-to-noise (S/N) ≥ 3 . The velocities where SiO(1–0) shows absorption features (see Fig. 4) have not been taken into account. The red-shifted emission does not show a clear trend, while the SiO(5–4)/SiO(1–0) ratio for the blue-shifted emission peaks in correspondence of A2, suggesting an increase of the SiO excitation conditions. Finally, in Fig. 8 we compare the SiO(5–4) profile observed with the IRAM 30-m antenna, with that obtained by integrating the SMA image over the IRAM beam (11''; blue histogram). The spectral shapes well match and, given the flux-scale uncertainties of the SMA (15%) and IRAM 30-m (10%), the line intensities also agree well, indicating that the SMA array recovers at least the 90% of the emission detected with the single-dish.

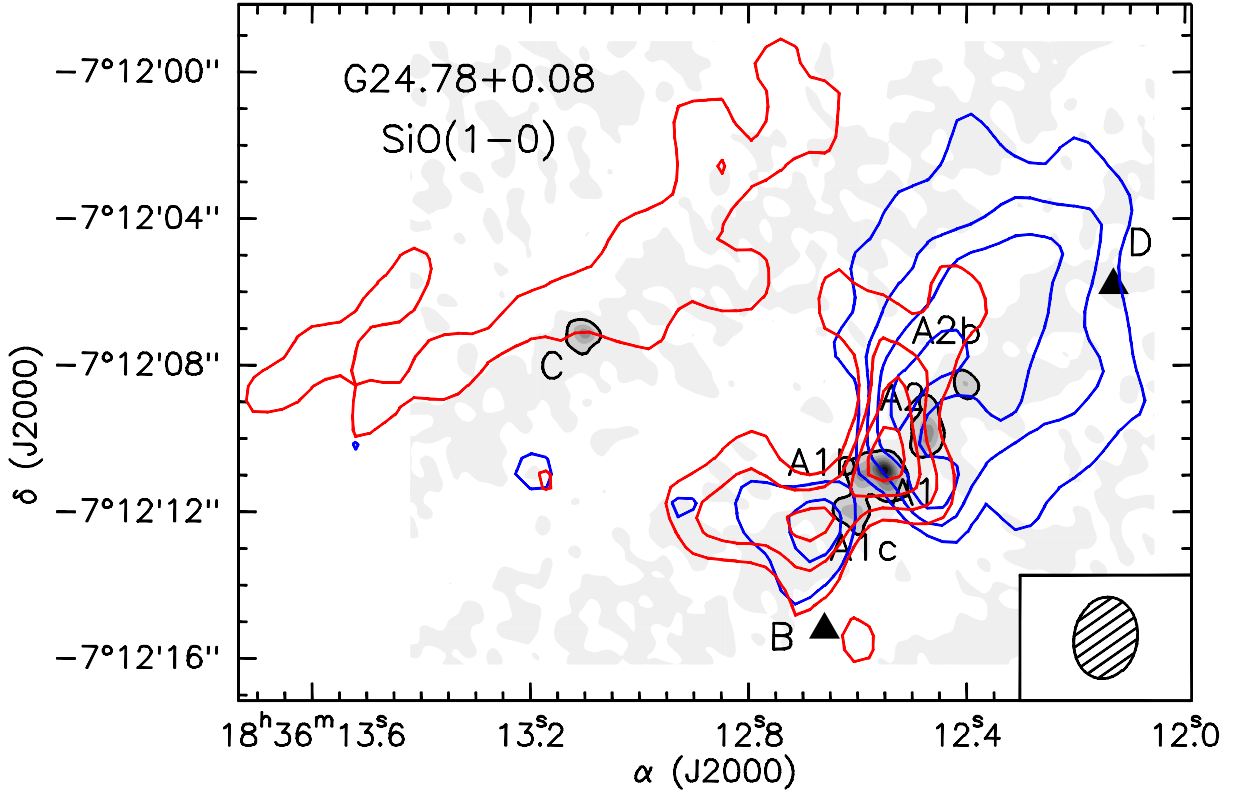


Fig. 2. Contour map of blue- and red-shifted SiO(1–0) VLA emission superimposed on the 1.3 mm continuum emission as observed at high angular resolution by Beltrán et al. (2011) using a very extended SMA configuration ($0''.55 \times 0''.44$). The sources of the G24.78+0.08 cluster are labelled following Furuya et al. (2002) and Beltrán et al. (2004, 2011). The SiO emission was averaged over the velocity intervals $(+80, +111)$ km s^{-1} and $(+111, +132)$ km s^{-1} for the blue- and red-shifted emission, respectively. The 1σ rms of the SiO maps is $1.2 \text{ mJy beam}^{-1} \text{ km s}^{-1}$. Contour levels range from 5σ by steps of 3σ . The filled ellipse in the bottom-right corner shows the synthesised beam (HPBW): $2''.2 \times 1''.7$ (PA = -15°).

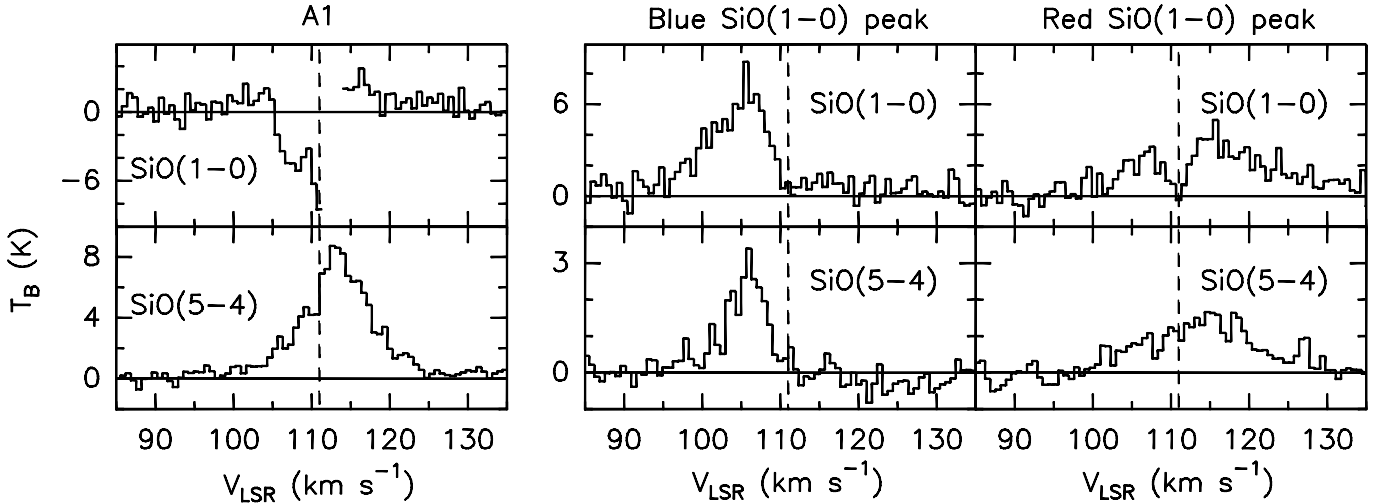


Fig. 4. Examples of SiO(1–0) and (5–4) line profiles (in brightness temperature T_B , scale) observed towards A1 (left panel) and the peak positions of the blue- and red-shifted (middle and right panel) SiO(1–0) line emission. Dashed lines mark the systemic velocity ($+111 \text{ km s}^{-1}$).

3.3. The origin of the outflow A

Which is the driving source of the outflow A? The VLA and SMA SiO images have been overlaid on the 1.3 mm continuum map obtained at sub-arcsecond angular resolution ($0''.55 \times 0''.44$) by Beltrán et al. (2011), which gives the best picture so far available of the YSO population in the G24.78+0.08 cluster. It is

possible to see that cores A1 and A2 are resolved into three (called A1, A1b, A1c) and two (A2, A2b) cores, respectively. By analysing the CO emission, Beltrán et al. (2011) suggested that the outflow A is actually powered by core A2, which is massive ($22 M_\odot$) and associated with a hot-core ($\sim 180 \text{ K}$) detected in CH_3CN , a typical hot-core tracer. The SiO images suggest that A1 is not the driving source of the outflow motions detected

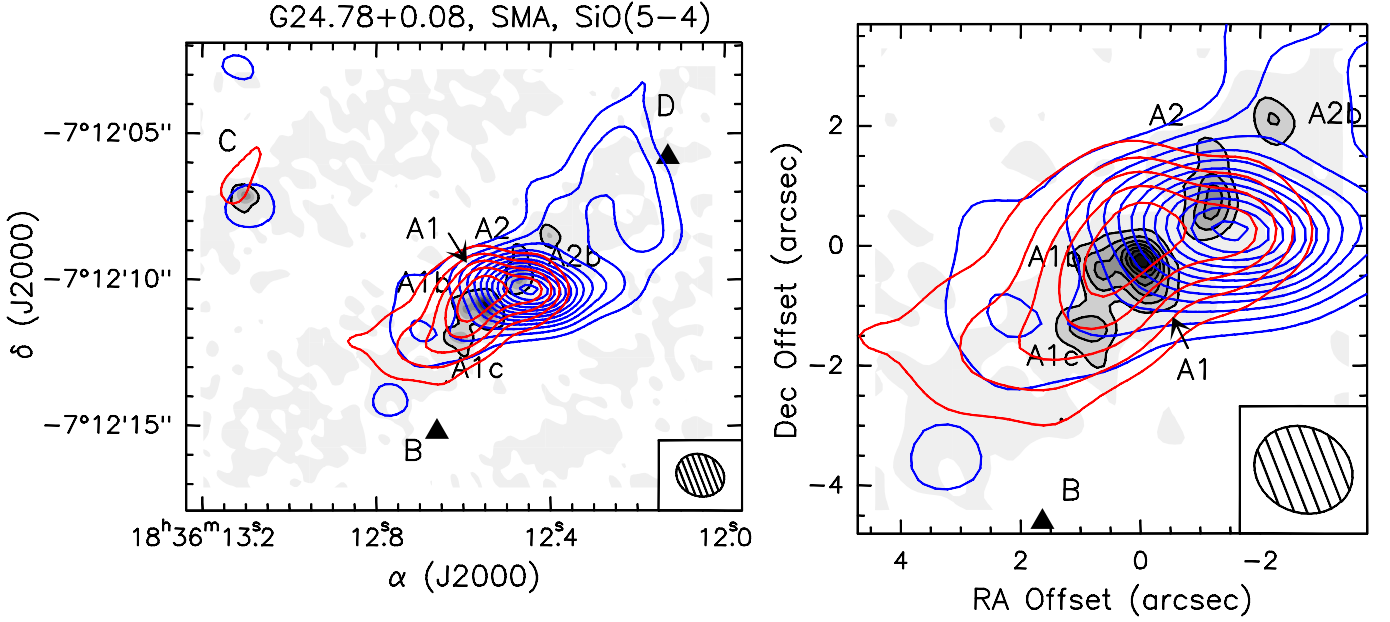


Fig. 6. Contour map of blue- and red-shifted SiO(5–4) SMA emission superimposed on the 1.3 mm continuum emission as observed at high angular resolution by Beltrán et al. (2011) using a very extended SMA configuration ($0''.55 \times 0''.44$). The Right panel reports a zoom-in of the central region. The sources of the G24.78+0.08 cluster are labeled following Furuya et al. (2002) and Beltrán et al. (2004, 2011). The SiO emission was averaged over the velocity intervals $(+89, +111)$ km s^{-1} and $(+111, +130)$ km s^{-1} for the blue- and red-shifted emission, respectively. The rms 1σ of the SiO maps is $18 \text{ mJy beam}^{-1} \text{ km s}^{-1}$. Contour levels range from 5σ by steps of 3σ . The filled ellipse in the bottom-right corner shows the synthesised beam (HPBW): $1''.7 \times 1''.4$ (PA = 67°).

so far. Given the presence of several YSOs in the region, we cannot exclude additional fainter outflows. However, the peaks of the SiO(5–4) emission suggest that the geometrical centre of outflow A, and thus its driving source, is located in the southern portion of the A2 core, which indeed is clearly elongated and probably hosts multiple YSOs. Additional evidence comes from the position-velocity (PV) diagram of the SiO(5–4) transition along the NW–SE axis (see Fig. 9), which seems to confirm that A1 cannot be the driving source. Interestingly, the average velocity of the SiO emission increases as a function of distance from the geometrical centre, suggesting gas acceleration. Figure 10 compares the PV diagram of SiO(5–4) with that derived from the CO(2–1) SMA data by Beltrán et al. (2011). We can clearly see that the CO emission (i) is completely absorbed by foreground material at low velocities and is affected by filtered extended emission, confirming the need of a tracer such as SiO to properly image the molecular outflow, and (ii) shows additional components with respect to what was traced by SiO. Indeed, bright CO emission is seen at $(-5'', +115 \text{ km s}^{-1})$, not traced by SiO, as well as weak emission at $(+2'', +113 \text{ km s}^{-1})$. In other words, the CO emission cannot be simply interpreted as an intensity-scaled version of the SiO emission. These findings are not surprising given what already found for the jets driven by Sun-like protostars, where, thanks to the smaller spatial scales that can be investigated, it is possible to see that CO traces not only the jet but also the walls of the cavity opened by the jet itself (e.g. Lee et al. 2007b, see their Fig. 5). In summary, the present SiO maps support a formation mechanism for massive stars similar to that of their low-mass counterparts, where jets, clearly traced by SiO emission, create outflows of swept-up ambient gas traced by CO. The possibility of having an SiO jet is also supported by the extremely high velocity (up to $\sim 70 \text{ km s}^{-1}$ with respect to the systemic velocity) of the SiO emission detected in the $J = 2-1$ and $3-2$ spectra thanks to the high

sensitivities provided at these frequencies by the 30-m antenna. Of course, in the present case, the angular resolution is not high enough to assess the occurrence of SiO jets. However, in analogy to the SiO jets in low-mass stars, one cannot rule out the possibility that the elongated SiO outflow does trace jet activity.

3.4. Other molecular species: the outflow and the hot core

The 2-GHz-wide LSB bandwidth used to trace SiO(5–4) emission with the SMA allowed us to serendipitously observe several lines of different molecular species, which are listed in Table 4 and shown in Fig. 11. In particular, the LSB spectrum is dominated by broad $\text{H}_2\text{S}(2_{2,0}-2_{1,1})$ emission, which confirms that hydrogen sulphide is an excellent tracer of molecular outflows (Codella et al. 2003, Gibb et al. 2004). Figure 12 shows the integrated blue- and red-shifted H_2S emission from outflow A, while Fig. 9 shows the corresponding PV diagrams.

Outflow A is clearly seen in the H_2S image, which suggests (like SiO) that the geometrical centre (and thus the driving source) is located in the southern portion of the A2 core. Interestingly, the H_2S outflow is definitely less collimated than the SiO(5–4) one, observed with the same angular resolution. H_2S and SiO show different behaviours also in the PV diagrams, where hydrogen sulphide does not show a clear increase of the average velocity with the distance from the driving source. These findings could be the signature of an additional fainter outflow driven by one of the A1+A2 YSOs that contributes to the observed emission. However, what we found agrees with an enhancement of the H_2S abundance as a consequence of the evaporation of the dust mantles in a shocked gas (e.g. van Dishoeck & Blake 1998), whereas SiO comes from a definitely smaller region that is directly associated with the primary jet, where the refractory dust cores are disrupted as well.

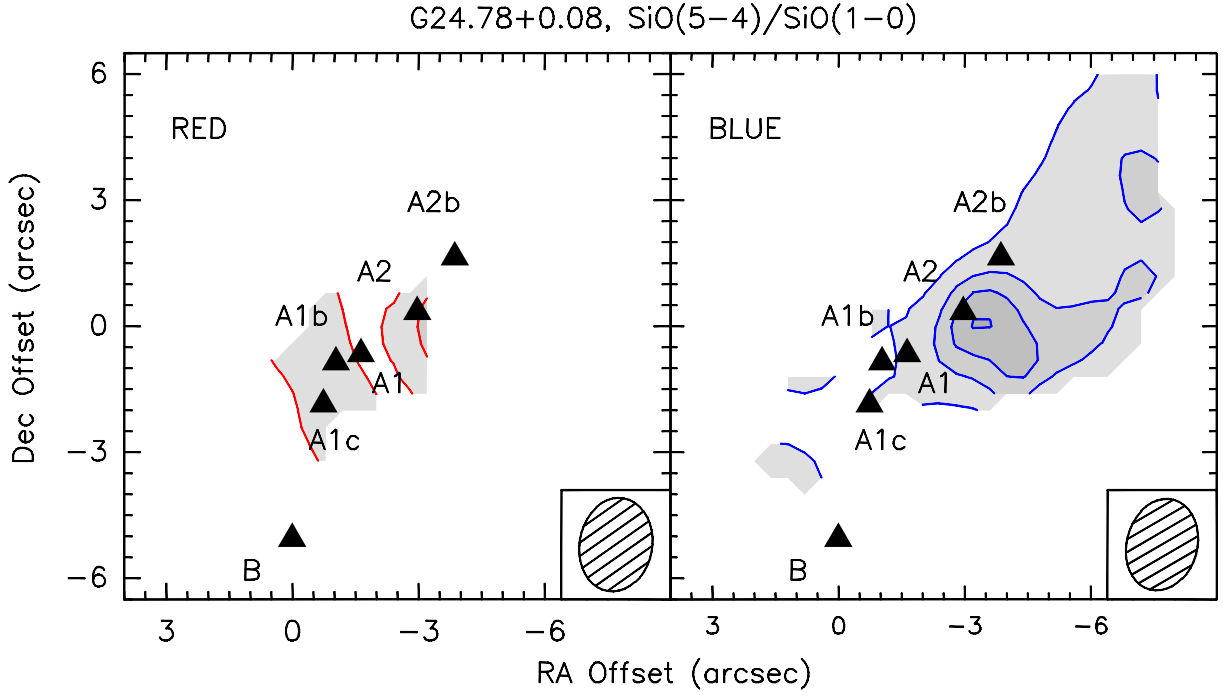


Fig. 7. SiO(5–4)/SiO(1–0) intensity ratio (brightness temperature, T_B , scale), derived where both emissions have an $S/N \geq 3$. For this comparison, the SMA image has been smoothed to the angular resolution of the VLA image. The velocities affected by SiO(1–0) absorption (see Fig. 4) have not been taken into account: right and left panels are for the blue (+89,+105 km s⁻¹) and red (+115,+130 km s⁻¹) emission, respectively. Contour levels range from 0.5 to 2.0 by steps of 0.5. The sources of the G24.78+0.08 cluster are labelled following Furuya et al. (2002) and Beltrán et al. (2004, 2011).

In addition to SiO and H₂S, we detected several high-excitation (E_u between 45 and 162 K) transitions of methanol isotopologues (see Table 4). Figure 11 shows the spectra observed towards the A2 position. The CH₃OH line profiles are narrower than those of SiO and H₂S and, although a weak component related to outflows cannot be excluded for ¹²CH₃OH, it appears that methanol emission is dominated here by gas heated by YSOs. Indeed, from Fig. 9 one clearly sees that the PV diagram of methanol, outlining a compact circular pattern, is significantly different from that of SiO. Most likely, the CH₃OH molecules trace the hot core A2 (already imaged by Beltrán et al. (2005)), and are released from dust mantles because of stellar irradiation. In particular, ¹³CH₃OH peaks at a position that matches the geometrical centre of the outflow well (see the solid vertical line in Fig. 9). Thus, the present observations suggest that a YSO lying in the SE of core A2 is heating the gas and driving the outflow A.

Finally, we also detected several lines in the SMA spectral window that are due to cyanoacetylene (in HCC¹³CN form) as well as to other complex molecular species usually considered as hot-core tracers: CH₃OCHO (methyl formate), C₂H₃CN (vinyl cyanide), and, tentatively, one transition of (CH₃)₂CO (acetone). Other complex species were reported by Beltrán et al. (2011, see their Table 1). Indeed, these emissions are characterised by high excitation (E_u in the 109–298 K range) and compact spatial distribution (see the C₂H₃CN in Fig. 9 as an example), indicating an association with the hot core traced by ¹³CH₃OH. Remarkable is the tentative detection of acetone, given that only recently this organic specie has been detected towards the hot molecular core Sagittarius B2(N-LMH) and in Orion BN/KL (Snyder et al. 2002, Friedel et al. 2005, Goddi et al. 2009).

4. Physical conditions as traced by SiO

4.1. SiO(1–0) absorption

From the SiO(1–0) absorption feature one can obtain an estimate of the excitation temperature of this transition. We assume that the absorption is due to the blue lobe of the outflow lying between the observer and the hypercompact HII region. Since the lobe is resolved in our maps, while the HII region is much smaller than the synthesised beam of the SiO images, the SiO(1–0) brightness temperature measured in the synthesised beam is a mixture of absorption (towards the HII region) and emission (from the rest of the beam):

$$\Omega_B T_B = (\Omega_B - \Omega_S) T_e + \Omega_S T_a, \quad (1)$$

where T_e and T_a are the brightness temperatures of the SiO(1–0) line in emission and absorption, while Ω_S and Ω_B are the solid angle subtended by the HII region and the synthesised beam of the SiO(1–0) map. Moreover, T_e and T_a are given by

$$T_e = T_{\text{ex}} (1 - e^{-\tau_e}) \quad (2)$$

$$T_a = (T_{\text{ex}} - T_{\text{HII}}) (1 - e^{-\tau_a}), \quad (3)$$

with T_{ex} excitation temperature of the $J=1-0$ transition and T_{HII} brightness temperature of the continuum emission from the hypercompact HII region. Here, we have assumed that T_{ex} is constant along the line of sight and across the region covered by the synthesised beam. After some algebra, one obtains the expression

$$T_B = T_{\text{ex}} (1 - e^{-\tau_e}) \left[1 - \frac{\Omega_S}{\Omega_B} \frac{e^{-\tau_a} - e^{-\tau_e}}{1 - e^{-\tau_e}} \right] - \frac{\Omega_S}{\Omega_B} T_{\text{HII}} (1 - e^{-\tau_a}). \quad (4)$$

G24.78+0.08 A

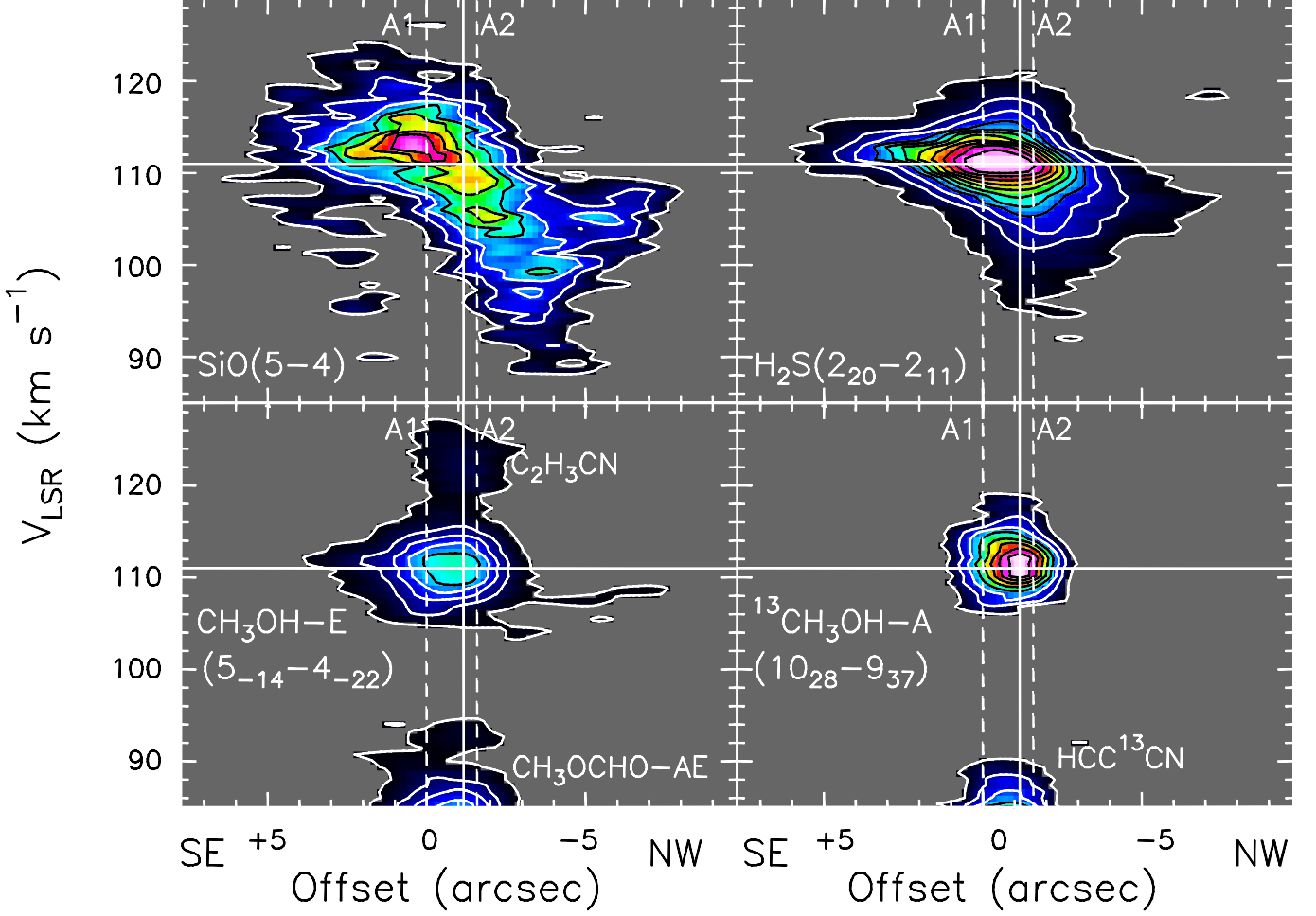


Fig. 9. Position-velocity cut of SiO(5–4), H₂S(2_{2,0}–2_{1,1}), CH₃OH-E(5_{-1,4}–4_{-2,2}), and ¹³CH₃OH-A(10_{2,8}–9_{3,7}) along the outflow A (PA = –40°). The position offsets are measured from the A1 position, positive towards northwest. The rms 1σ is 20 mJy beam⁻¹. Contour levels range from 3σ by steps of 3σ for SiO and ¹³CH₃OH-A, and from 3σ by steps of 10σ for H₂S and CH₃OH-E. Dashed vertical lines mark the position of the A1 and A2 YSOs, while the solid vertical line is for the average peak position of the typical hot-core tracers (see text). Solid horizontal line shows the systemic velocity (+111.0 km s⁻¹).

We note that the Ω_B is relatively small compared to the size of the outflow lobe, and hence the opacity should not depend significantly on the line of sight. Also, for obvious reasons, the HII region either lies behind the lobe or is enshrouded by it. Therefore, $\tau_a \leq \tau_e$ and $0 \leq \frac{e^{-\tau_a} - e^{-\tau_e}}{1 - e^{-\tau_e}} < 1$. Since $\frac{\Omega_S}{\Omega_B} \ll 1$, Eq. (4) can be written as

$$T_B \approx T_{\text{ex}}(1 - e^{-\tau_e}) - \frac{\Omega_S}{\Omega_B} T_{\text{HII}}(1 - e^{-\tau_a}). \quad (5)$$

Most likely, the absorption and emission lines of sight are crossing similar amounts of gas, and we hence make the additional assumption that $\tau_a \approx \tau_e$. By replacing Eq. (2) into Eq. (5), one can finally obtain an expression for T_{ex} :

$$T_{\text{ex}} = \frac{\Omega_S}{\Omega_B} T_{\text{HII}} \frac{T_e}{T_e - T_B}. \quad (6)$$

From our observations we measure absorption with $T_B \approx -6$ K in a beam of $\Omega_B = 4.24$ arcsec², while from the data of Beltrán et al. (2007) one obtains $\Omega_S \approx 0.0554$ arcsec² and a source-averaged brightness temperature of the HII region at 7 mm $T_{\text{HII}} \approx 960$ K. An estimate of T_e can be obtained from the

SiO(1–0) spectra one beam away from the absorption peak: $T_e \approx 3$ –6 K. With these numbers we obtain $T_{\text{ex}} \approx 4$ –8 K. The brightness temperature of the continuum emission measured at 7 mm towards the HII region in our images is ~ 12 K, i.e. comparable to the value ($\frac{\Omega_S}{\Omega_B} T_{\text{HII}} \approx 12$ K) estimated applying beam dilution to the high-resolution measurement of Beltrán et al. (2007): this proves that basically the entire continuum emission in our beam is due to free-free emission from the ionised gas, while dust emission is negligible.

4.2. LVG analysis

We ran the RADEX non-LTE model (van der Tak et al. 2007) with the rate coefficients for collisions with H₂ reported by Turner et al. (1992) using the escape probability method for a plane-parallel geometry to fit the observed SiO line ratios and brightness. We explored H₂ densities from 10² to 10⁸ cm⁻³, kinetic temperatures T_{kin} from 50 to 500 K, and an LVG optical depth parameter $n(\text{SiO})/(dV/dz) = N_{\text{SiO}}/\Delta V$ ranging from 10¹² to 10¹⁷ cm⁻² (km s⁻¹)⁻¹, i.e. from the fully optically thin to the

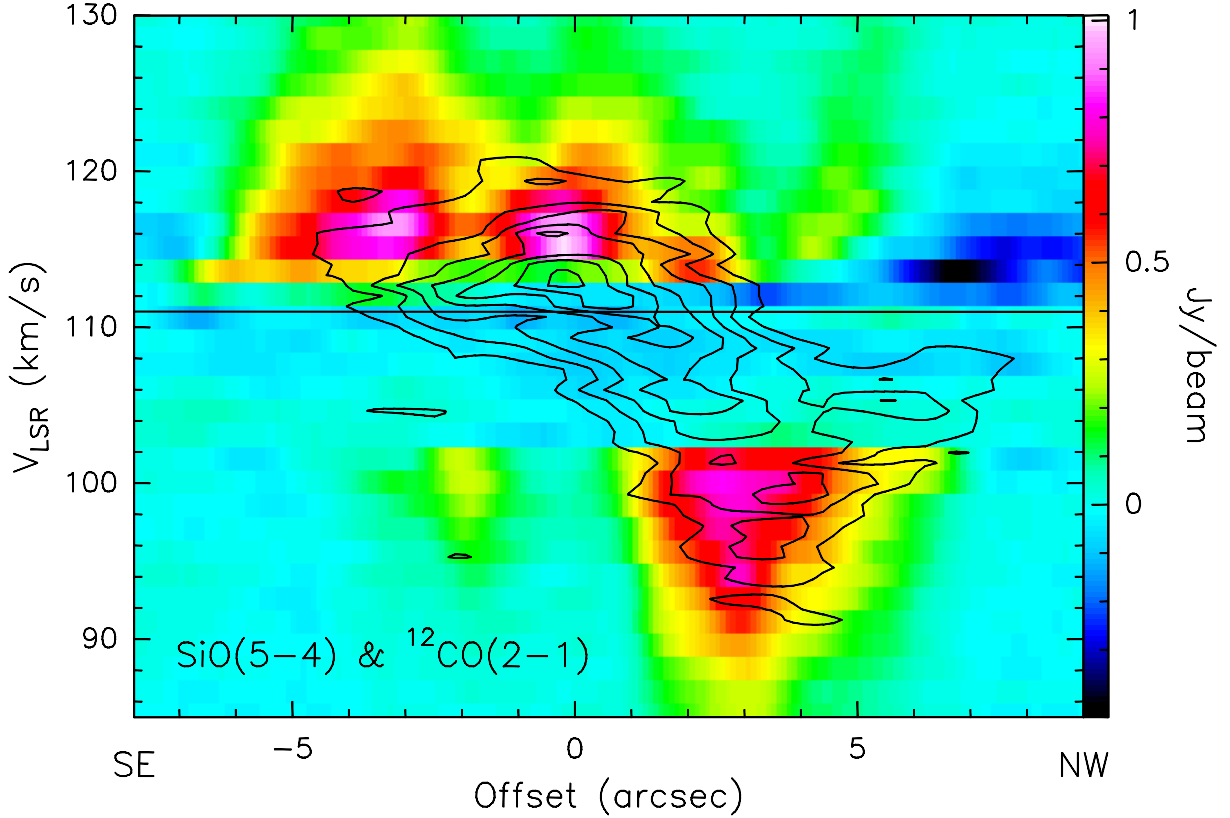


Fig. 10. Comparison between the position-velocity cut of SiO(5–4), black contours, and that of CO(2–1) in colours, derived along the outflow A (PA = -40°) using the CO dataset presented by Beltrán et al. (2011). The solid horizontal line shows the systemic velocity ($+111.0 \text{ km s}^{-1}$).

optically thick regime. We used an FWHM linewidth of 10 km s^{-1} , as suggested by the SiO spectra (see Fig. 4).

As a first step, we modelled the SiO emission observed with the IRAM 30-m telescope, using the SiO(2–1) and (5–4) transitions, which are sensitive to similar excitation conditions (see Table 1) as the lines observed with the interferometers (discussed below). The low-J SiO lines, as already learned from previous studies of low-mass protostellar systems (e.g. Cabrit et al. 2007 and references therein), are not very sensitive to kinetic temperature. Figure 13 thus reports the solutions for the observed SiO(5–4)/SiO(2–1) intensity ratio at the typical red- ($+116 \text{ km s}^{-1}$) and blue-shifted ($+106 \text{ km s}^{-1}$) emission in the n_{H_2} – $N(\text{SiO})$ plane and for two extreme temperatures: 50 and 500 K. The observed intensity ratio was corrected for beam dilution assuming an emitting source of $7''$, which is representative of the sizes of the outflows imaged with the VLA and SMA. To show how much the results depend on this assumption on emitting size, we also report the solutions for a smaller size (i.e. $3''$), which is the typical size of the brightest SiO clumps in G24. The dashed contours take into account the uncertainties associated with the intensity ratio. The 30-m spectra do not provide any constraint on the kinetic temperature and column density, while densities of below 10^5 cm^{-3} can be inferred.

On the other hand, we can obtain tight constraints on volume and column densities by analysing the SiO emission observed with the VLA and SMA arrays, after degrading the SMA map to the angular resolution of the VLA image. Figures 14 and 15 report the solutions for the observed SiO(1–0) and SiO(5–4) brightness temperatures at the same red- ($+116 \text{ km s}^{-1}$) and blue-shifted ($+106 \text{ km s}^{-1}$) velocities investigated using the 30-m spectra. We modelled the emission observed towards three

positions: A1 (Fig. 14), as well as where the J=1–0 emission is only weakly affected by absorption, i.e. at the position of the red- and blue-shifted SiO(1–0) emission peaks (Fig. 15). As reported in Table 3, the positions of the red-shifted peak as traced by SiO(1–0) and (5–4), hence once considered the angular resolutions, agree well. We report the solutions found for the same kinetic temperatures used above to model the 30-m emission (50 and 500 K). We plot in black in Fig. 14 the contours corresponding to the the excitation temperature of the SiO(1–0) line estimated in Sect. 4.1 from the SiO(1–0) absorption feature observed towards A1.

In practice, the present LVG plots indicate for the three positions (i) volume densities between 10^3 and 10^5 cm^{-3} , and (ii) well-constrained SiO column density, in the 0.5 – $1 \cdot 10^{15} \text{ cm}^{-2}$ range. These solutions are consistent with what was found using the 30-m IRAM SiO(5–4) and (2–1) spectra. Nisini et al. (2007) performed an LVG analysis of SiO emission towards the nearby prototypical Class 0 low-mass objects L1148 and L1157, using single-dish (IRAM, JCMT) data on angular scales of $10''$. In that case as well, no tight constraints have been obtained for the kinetic temperature, whereas the volume densities were found to be between 10^5 and 10^6 cm^{-3} . Moreover, Gusdorf et al. (2008a) modelled the SiO emission from L1157 using a C-shock code, which led to pre-shocked densities of 10^4 – 10^5 cm^{-3} . Thus, although completely different spatial scales are involved, the volume densities here inferred for G24 (10^3 – 10^5 cm^{-3}) appear to be consistent with those derived for L1448 and L1157.

Assuming that the physical conditions reported above are representative of the whole SiO outflow (including where SiO(1–0) emission is affected by absorption), using a volume density of 10^4 cm^{-3} , the inferred size of the lobes ($7''$), and the

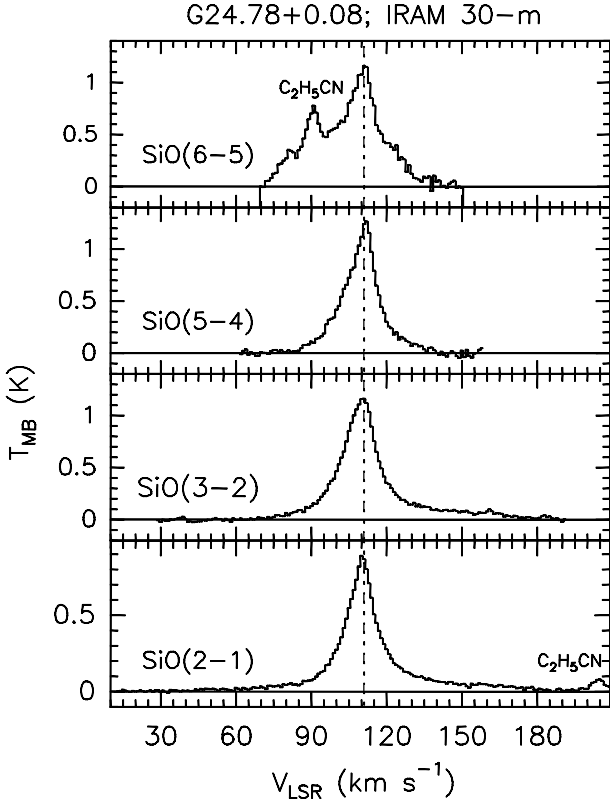


Fig. 3. SiO line profiles (in main-beam temperature, T_{MB} , scale) observed with the IRAM 30-m antenna towards G24.78+0.08. The dashed lines stand for the systemic velocity ($+111.0 \text{ km s}^{-1}$). Two ethyl cyanide ($\text{C}_2\text{H}_5\text{CN}$) emission lines have been serendipitously detected at 86819.85 MHz ($10_{1,10}-9_{1,9}$; $E_u=24 \text{ K}$; bottom panel), and at 260535.69 MHz ($29_{5,25}-28_{5,24}$; $E_u=215 \text{ K}$; upper panel), blended with the SiO(6-5) blue wing.

G24 distance (7.7 kpc), the corresponding outflow mass is $\sim 40 M_{\odot}$. This implies, according to Beuther et al. (2002), Zhang et al. (2001, 2005), and López-Sepulcre et al. (2009, see their Fig. 5), a luminosity for the driving source of the SiO outflow of a few $10^4 L_{\odot}$, corresponding to a late O-type ZAMS YSO (e.g. Panagia 1973). If we conservatively assume $n_{\text{H}_2} = 10^3 \text{ cm}^{-3}$, the driving source is still a massive YSO, corresponding to a B2 spectral type. However, for consistency purposes, we cross-checked the outflow masses using the estimates of SiO column density and assuming a given SiO abundance relative to H_2 . The latter has a large uncertainty since SiO can be greatly enhanced in shocks. Assuming typical abundances of $10^{-8}-10^{-7}$ (i.e. 4–5 orders of magnitude greater than that in dark clouds, 10^{-12} , Ziurys et al. 1989), we inferred volume densities between 10^4 and 10^5 cm^{-3} , and thus again masses ($\sim 40-400 M_{\odot}$) in agreement with an outflow driven by a late O-type ZAMS YSO.

5. Conclusions

We conducted a multiline SiO survey towards the G24.78+0.08 region, which is an excellent laboratory to study the process of high-mass star formation, because it is associated with YSOs in different evolutionary stages. After preliminary IRAM 30-m single-dish runs, we obtained high angular resolution images using the VLA and SMA interferometers. The main results can be summarised as follows:

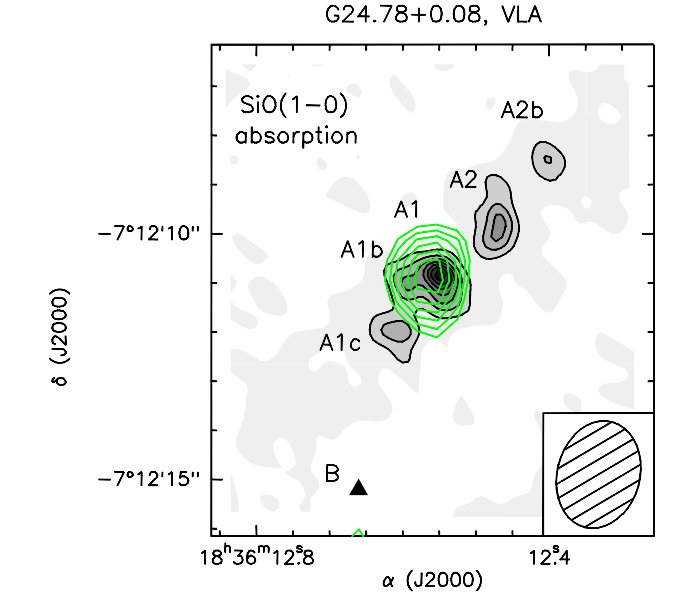


Fig. 5. Zoom-in of the central region of G24.78+0.08, where the cluster of A1-A2 continuum sources (grey scale) has been mapped at high angular resolution by Beltrán et al. (2011) using a very extended SMA configuration ($0'.55 \times 0'.44$). The spatial distribution of the blue-shifted (from $+106$ to $+110 \text{ km s}^{-1}$) absorption (see Fig. 4) observed towards A1 is reported by the green contours. Contour levels range from -10σ to -3σ by steps of 1σ ($0.3 \text{ mJy beam}^{-1} \text{ km s}^{-1}$). The filled ellipse in the bottom-right corner shows the synthesised beam (HPBW): $2''.2 \times 1''.7$ (PA = -15°).

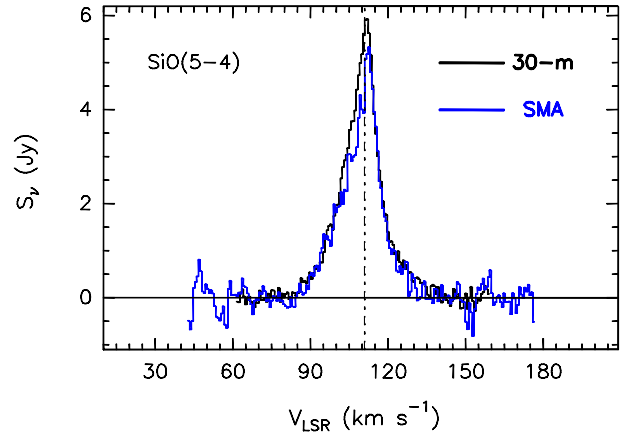


Fig. 8. Comparison between the SiO(5-4) line profile (in flux density, S_{ν} , scale) observed with the IRAM 30-m antenna (black) and the spectrum obtained from the SMA data (blue) by integrating over a region equal to the IRAM 30-m beam ($11''$). For this comparison the IRAM 30-m spectrum has been resampled to the spectral resolution of the SMA data (0.67 km s^{-1}). The dashed lines stand for the systemic velocity ($+111.0 \text{ km s}^{-1}$).

1. High-velocity SiO emission (up to 25 km s^{-1} w.r.t. the systemic velocity, $+111 \text{ km s}^{-1}$) reveals two collimated outflows driven by the A2 and C millimeter continuum massive cores. On the other hand, no SiO emission has been detected towards more evolved young stellar objects associated with an UCHII region (core B) or driven by the hypercompact (core A1) HII regions. Moreover core D shows no SiO emission,

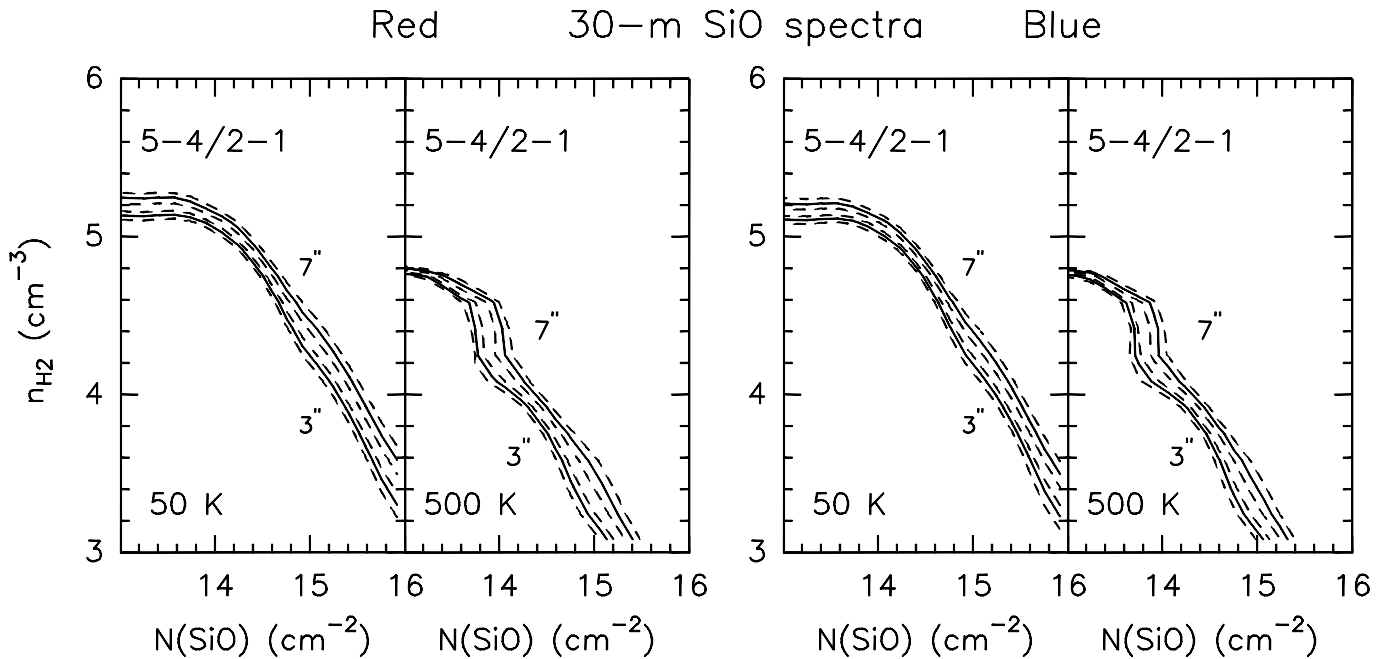


Fig. 13. Analysis of the SiO red-shifted line emission in the G24.78+0.08 outflow A observed with the IRAM 30-m antenna. The solutions for the observed SiO(5–4)/SiO(2–1) intensity ratio are shown in the n_{H_2} – $N(\text{SiO})$ plot for non-LTE (RADEX) plane-parallel models at the labeled kinetic temperatures. Solid contours are for the measured ratios at the typical red- (+116 km s^{−1}) and blue-shifted (+106 km s^{−1}) velocities, after correction for a beam dilution derived assuming a source size of 3'' and 7'' (see text). The SiO(5–4)/SiO(2–1) ratios are 0.21 (3''; +116 km s^{−1}), 0.19 (3''; +106 km s^{−1}), 0.27 (7''; +116 km s^{−1}), and 0.30 (7''; +106 km s^{−1}). Dashed contours take into account the uncertainties.

confirming its quiescent nature, without any signature of star formation.

2. The LVG analysis of the SiO emission reveals high-density gas (10^3 – 10^5 cm^{−3}), with clearly constrained SiO column densities ($\sim 10^{15}$ cm^{−2}). The average velocity of the SiO emission increases as a function of distance from the driving source, which suggests gas acceleration. Although the angular resolution is not high enough to demonstrate the occurrence of SiO jets, if we assume the standard approach that SiO is tracing shocks inside jets, it is reasonable to associate the observed collimated SiO structures with jet activity.
3. The driving source of the A2 outflow (i) has an estimated luminosity of $\geq 10^4 L_{\odot}$, which is typical of a late O-type star, and (ii) is located at the centre of a hot molecular core (traced in the present data set by emission from methyl formate, vinyl cyanide, cyanoacetylene, and acetone) that rotates on a plane perpendicular to the outflow main axis.
4. To our knowledge, we obtained one of the first interferometric images of an SiO jet-like outflow from young $\geq 10^4 L_{\odot}$ stars. High spatial resolution maps of SiO high-velocity emission driven from young $\geq 10^4 L_{\odot}$ stars have been so far obtained towards IRAS18264–1152, 18566+0408, 20126+4104, and 23151+5912 (Cesaroni et al. 1999; Qiu et al. 2007; Zhang et al. 2007). IRAS20126+4104 is probably the best example of a jet from a massive YSO so far observed; it is traced by SiO, H₂, and [FeII] emission (Caratti o Garatti et al. 2008). To conclude, the present SiO observations support the theory that O-type stars form according to a core accretion model, i.e. via a scaled-up picture typical of Sun-like star formation, where jets, well-traced by SiO emission, create outflows of accumulated and accelerated ambient gas that in turn is well traced by CO.

Acknowledgements. We wish to thank the IRAM staff for the 30-m observations performed in service mode. We are grateful to S. Cabrit for useful discussion and suggestions. We also thank the anonymous referee for comments and suggestions, which improved the work.

References

- Bachiller R., Pérez Gutiérrez M., Kumar M.S.N., & Tafalla M. 2001, A&A 372, 899
- Beltrán M.T., Cesaroni R., Neri R., et al. 2004, ApJ 601, L187
- Beltrán M.T., Cesaroni R., Neri R., et al. 2005, A&A 435, 901
- Beltrán M.T., Cesaroni R., Codella C., et al. 2006, Nature 443, 427
- Beltrán M.T., Cesaroni R., Moscadelli L., & Codella C. 2007 A&A 471, L13
- Beltrán M.T., Cesaroni R., Zhang Q., et al. 2011, A&A 532, A91
- Bonnell I.A., Larson R.B., & Zinnecker H., 2007, Protostars & Planets V, eds. B. Reipurth, D. Jewitt, & K. Keil (University of Arizona Press), 149
- Beuther H., Schilke P., Sridharan T.K., et al. 2002, A&A 383, 892
- Briggs D. 1995, Ph.D. Thesis, New Mexico Inst. Mining & Tech.
- Caratti o Garatti A., Froebrich D., Eislöffel J., Giannini T., & Nisini B. 2008, A&A, 485, 137
- Cabrit S., Codella C., Gueth F., et al. 2007, A&A 468, L29
- Cesaroni R., Felli M., Jenness T., et al. 1999, A&A 345, 949
- Cesaroni R., Codella C., Furuya R.S., & Testi L. 2003, A&A 401, 227
- Cesaroni R., Neri R., Olmi L., et al. 2005, A&A 434, 1039
- Codella C., Testi L., & Cesaroni R. 1997, A&A 325, 282
- Codella C., Bachiller R., Benedettini M., & P. Caselli 2003, MNRAS 341, 707
- Codella C., Cabrit S., Gueth F., et al. 2007, A&A 462, L53
- Friedel D.N., Snyder L.E., Remijan A.J., & Turner B.E. 2005, ApJ 632, L95
- Furuya R.S., Cesaroni R., Codella C., Testi L., Bachiller R., & Tafalla M. 2002, A&A 390, L1
- Gibb A.G., Wyrowski F., & Mundy L.G. 2004, ApJ 616, 301
- Goddi C., Greenhill L.J., Humphreys E.M.L., et al. 2009, ApJ 691, 1254
- Gusdorf A., Cabrit S., Flower D.R., & Pineau Des Forêts G. 2008a, A&A 482, 809
- Gusdorf A., Pineau Des Forêts G., Cabrit S., & Flower D.R. 2008b, A&A 490, 695
- Hunter T.R., Testi L., Zhang Q., & Sridharan T.K. 1999, AJ 118, 477
- Lee C.-F., Ho P.T.P., Beuther H., et al. 2007a, ApJ 659, L499
- Lee C.-F., Ho P.T.P., Palau A., et al. 2007b, ApJ 670, 1188

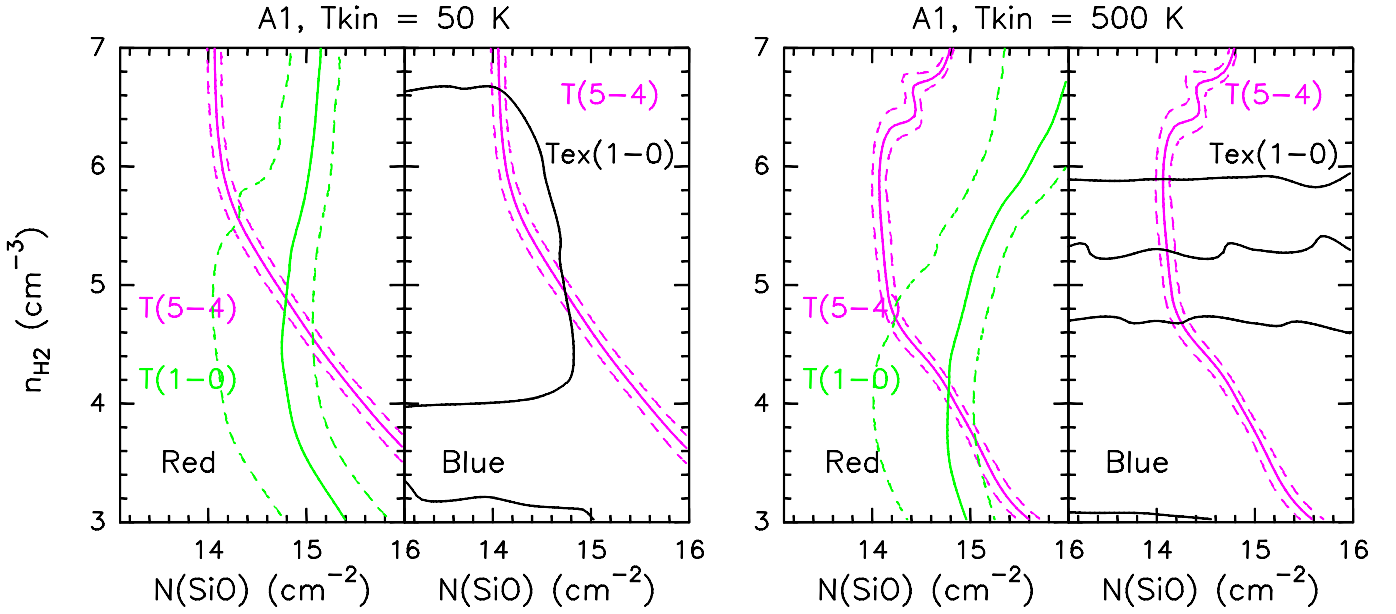


Fig. 14. Analysis of the SiO line blue- and red-shifted emissions towards A1 as observed with VLA and SMA (convolved to the angular resolution of the VLA image). The solutions for the observed SiO(1–0) and SiO(5–4) brightness temperatures (solid lines) at the typical red- (+116 km s^{−1}) and blue-shifted (+106 km s^{−1}) velocities are shown in the n_{H_2} – $N(\text{SiO})$ plane for non-LTE (RADEX) plane-parallel models at the labelled kinetic temperatures. Dashed lines are for the uncertainties. The SiO(5–4) brightness temperatures are 4.4 K (+116 km s^{−1}) and 4.3 K (+106 km s^{−1}), while the SiO(1–0) brightness temperature is 4.0 K (+116 km s^{−1}). Given the blue-shifted absorption observed towards A1, we plot in black the solutions corresponding to the derived SiO(1–0) excitation temperature (≈ 6 K, see Sect. 4.1).

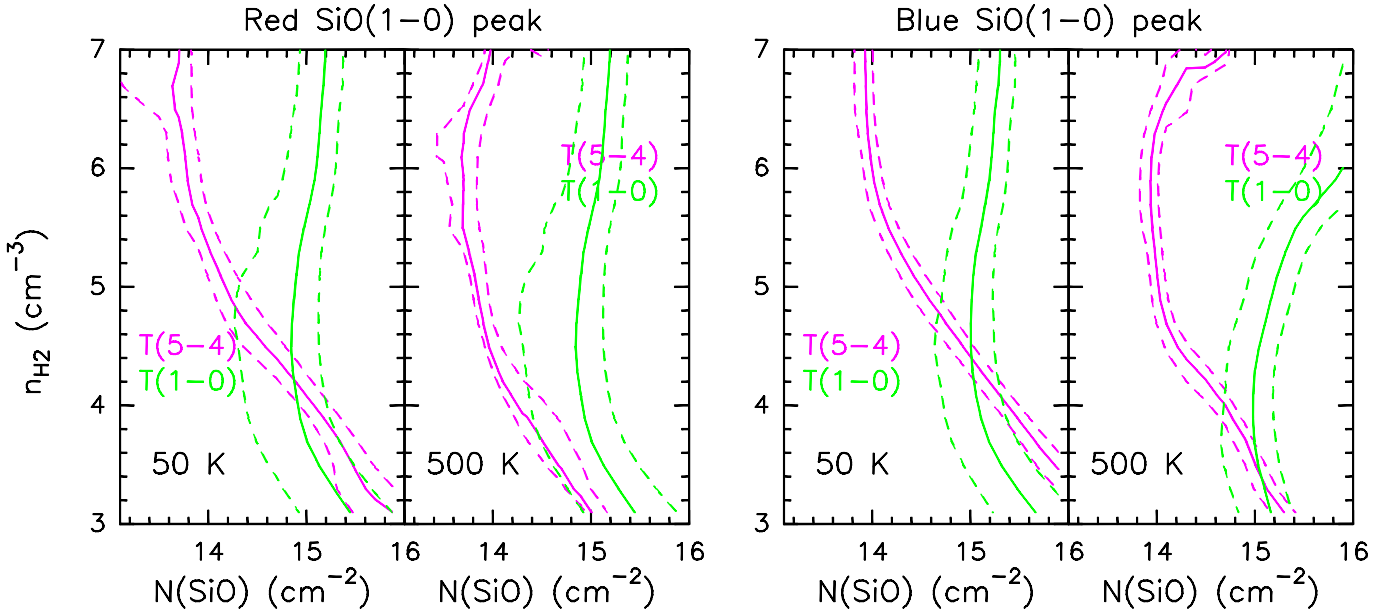


Fig. 15. Analysis of the SiO line blue- and red-shifted emissions towards the corresponding emission peaks of the SiO(1–0) map (see text), as observed with VLA and SMA (convolved to the angular resolution of the VLA image). The solutions for the observed SiO(1–0) and SiO(5–4) brightness temperatures at the typical red- (+116 km s^{−1}) and blue-shifted (+106 km s^{−1}) velocities are shown in the n_{H_2} – $N(\text{SiO})$ plane for non-LTE (RADEX) plane-parallel models at the labelled kinetic temperatures. The SiO(1–0) brightness temperatures are 4.7 K (+116 km s^{−1}) and 6.1 K (+106 km s^{−1}), while the SiO(5–4) brightness temperatures are 1.1 K (+116 km s^{−1}) and 2.9 K (+106 km s^{−1}). Dashed lines are for the uncertainties.

López-Sepulcre A., Codella C., Cesaroni R., Marcelino N., & Walmsley C.M. 2009 A&A 499, 811
 McKee C.F., & Tan J.C. 2002, Nature 416, 59
 McKee C.F., & Tan J.C. 2003, ApJ 585, 850
 Moscadelli L., Goddi C., Cesaroni R., Beltrán M.T., & Furuya R.S. 2007, A&A 472, 867

Müller H.S.P., Schöier F.L., Stutzki J., & Winnewisser G. 2005, J.Mol.Struct. 742, 215
 Panagia N. 1973, AJ 78, 929
 Pickett H.M., Poynter R.L., Cohen E.A., Delitsky M.L., Pearson J.C., and Müller H.S.P. 1998, J. Quant. Spectrosc. & Rad. Transfer, 60, 883
 Qui K., Zhang Q., Beuther H., & Yang J. 2007, ApJ 654, 361

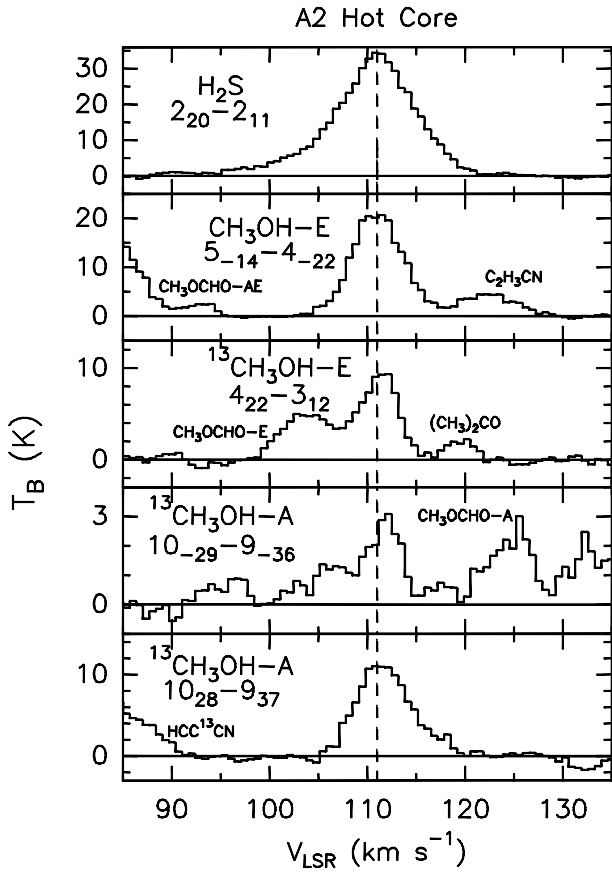


Fig. 11. SiO, H₂S, CH₃OH, and ¹³CH₃OH line profiles (in brightness temperature, T_B , scale) observed towards the A2 hot core with the SMA. The dashed lines denote the systemic velocity ($+111 \text{ km s}^{-1}$). Several high-excitation lines due to typical tracers of hot-core chemistry (methyl formate, acetone, vinyl cyanide, cyanoacetylene) have also been detected (see Table 4).

G24.78+0.08, SMA, H₂S($2_{20}-2_{11}$)

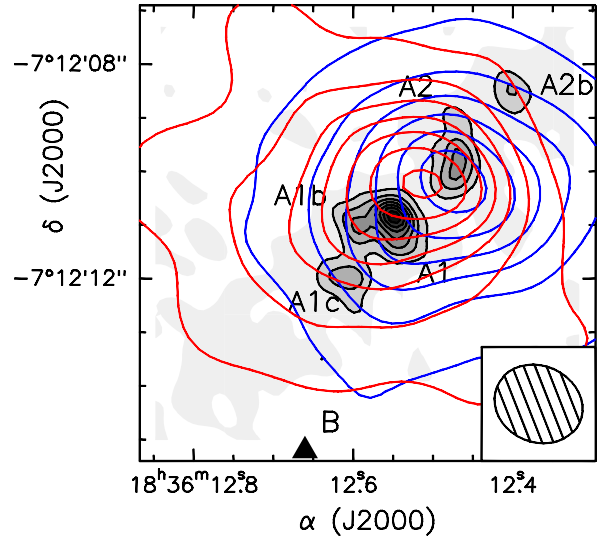


Fig. 12. Contour map of blue- and red-shifted H₂S($2_{2,0}-2_{1,1}$) SMA emission superimposed on the 1.3 mm continuum emission as observed at high angular resolution by Beltrán et al. (2011) using a very extended SMA configuration ($0'.55 \times 0'.44$). The sources of the G24.78+0.08 cluster are labelled following Furuya et al. (2002) and Beltrán et al. (2004, 2011). The H₂S emission was averaged over the velocity intervals $(+94, +111) \text{ km s}^{-1}$ and $(+111, +124) \text{ km s}^{-1}$ for the blue- and red-shifted emission, respectively. The rms 1σ is $18 \text{ mJy beam}^{-1} \text{ km s}^{-1}$. Contour levels range from 5σ by steps of 10σ . The filled ellipse in the bottom-right corner shows the synthesised beam (HPBW): $1'.7 \times 1'.4$ (PA = 67°).

- Sault R.J., Teuben P.J., & Wright M.C.H. 1995, in ASP Conf. Ser. 77: Astronomical Data Analysis Software and Systems IV, 433
 Schilke P., Walmsley C.M., Pineau des Forêts G., & Flower D.R. 1997, A&A 321, 293
 Snyder L.E., Lovas F.J., Mehringer D.M., et al. 2002, ApJ, 578, 245
 Turner B.E., Chan K.W., Green S., & Lubowich D.A. 1992, ApJ 399, 114
 van der Tak F.F.S., Black J.H., Schøier F.L., et al. 2007, A&A 468, 627
 van Dishoeck E.F., & Blake G.A., 1998, ARA&A 36, 317
 Vig S., Cesaroni R., Testi L., Beltrán M.T., & Codella C. 2008, A&A, 488, 605
 Zhang Q., Hunter T.R., Brand J., et al. 2001, ApJ 552, L167
 Zhang Q., Hunter T.R., Brand J., et al. 2005, ApJ 625, 864
 Zhang Q., Sridharan T.K., Hunter T.R., et al. 2007, A&A 470, 269
 Ziurys L.-M., Friberg P., & Irvine W.M. 1989, ApJ 343, 201